X-ray imaging with gaseous detectors using the VMM3a and the SRS

Scharenberg, L.

2021-09-21

Contents lists available at ScienceDirect

Nuclear Inst. and Methods in Physics Research, A

X-ray imaging with gaseous detectors using the VMM3a and the SRS

L. Scharenberg [a,b,*], J. Bortfeldt [c], F. Brunbauer [a], K. Desch [b], F. Garcia [d], M. Hracek [a,e],
D. Janssens [a,f], M. Lisowska [a,g], M. Lupberger [b], H. Muller [a], H. Natal da Luz [e], E. Oliveri [a],
D. Pfeiffer [h,a,i], H. Pulkkinen [a,j], L. Ropelewski [a], J. Samarati [h,a], M. van Stenis [a], A. Utrobicic [a],
R. Veenhof [a,k]

[a] European Organization for Nuclear Research (CERN), 1211 Geneva 23, Switzerland
[b] Physikalisches Institut, University of Bonn, Nußallee 12, 53115 Bonn, Germany
[c] Department for Medical Physics, Ludwig Maximilian University of Munich, Am Coulombwall 1, 85748 Garching, Germany
[d] Helsinki Institute of Physics, P.O. Box 64, FI-00014 University of Helsinki, Finland
[e] Institute of Experimental and Applied Physics, Czech Technical University in Prague, Husova 240/5, 110 00 Prague 1, Czech Republic
[f] Physics Department, Vrije Universiteit Brussel, Pleinlaan 2, 1050 Brussels, Belgium
[g] Wrocław University of Science and Technology, Wybrzeże Wyspiańskiego 27, 50-370 Wrocław, Poland
[h] European Spallation Source ERIC (ESS), Box 176, SE-221 00 Lund, Sweden
[i] University of Milano-Bicocca, Department of Physics, Piazza della Scienza 3, 20126 Milan, Italy
[j] VR Group, Radiokatu 3, 00240 Helsinki, Finland
[k] Bursa Uludağ University, Görükle Kampusu, 16059 Niüfer/Bursa, Turkey

ARTICLE INFO

ABSTRACT

The integration of the VMM3a Application-Specific Integrated Circuit (ASIC) into RD51's Scalable Readout System (SRS) provides a versatile tool for the readout of Micro-Pattern Gaseous Detectors (MPGDs). With its self-triggered high-rate readout, its analogue part that allows to get information on the deposited energy in the detector, and its so-called neighbouring-logic that allows to recover information on the charge distribution, this new system has features of particular interest for digital X-ray imaging. In the present article, we want to emphasise the capabilities of VMM3a/SRS by presenting results of X-ray imaging studies. We will highlight the advantages on the energy and the spatial resolution provided by the neighbouring-logic. In the first part, we focus on spatial resolution studies. We show how segmented readout structures introduce a repeating pattern in the distribution of the reconstructed positions (using the centre-of-gravity method) and how this behaviour can be mitigated with the neighbouring-logic. As part of these studies, we explore as well an alternative position reconstruction algorithm. In the second part of the article, we present the energy resolution studies.

1. Introduction

Particle detectors have a wide range of applications, also beyond (high energy) physics experiments, e.g. in medicine, in material science, or to investigate cultural heritage sites and assets (e.g. [1–3]). In case of (digital) imaging applications and particle tracking, it is important to acquire data that allow a precise reconstruction of the incident particle's position and trajectory. A prominent example of devices achieving excellent spatial resolutions are semiconductor detectors. Spatial resolutions of approximately $43\,\mu m$ FWHM (23 line pairs per millimetre (LP/mm) at $10\,\%$ MTF, see Section 3.4.1 for the terminology) for X-ray imaging [4] and $1.6\,\mu m$ for tracking with a beam telescope [5] are achieved. In both given examples, the semiconductor sensors have been mounted to a Medipix or a Timepix Application-Specific Integrated Circuit (ASIC) featuring 256×256 pixels with $55\,\mu m$ pitch, covering an area of about $2\,cm^2$ [6].

Among gaseous detector, Micro-Pattern Gaseous Detectors (MPGDs) achieve high spatial resolutions. While the resolution cannot meet the values reported for semiconductor-based detectors, MPGDs provide different important attributes for imaging and tracking: radiation hardness and large area coverage up to (hundreds) of square metres [7]. To be capable of preserving good spatial resolutions over a large area (around 300 to $400\,\mu m$ FWHM for imaging), MPGDs use highly segmented readout structures, e.g. thin strips [8,9] or small pads [10] with a pitch of hundreds of micrometres.

Connected to these structures are dedicated electronics, to process and digitise the signals produced in the detector, defining also the acquisition rate. Driven by the requirements for future collider experiments and beyond, new readout electronics are developed, pushing their capabilities to new frontiers. A prominent example is the ATLAS

New Small Wheel Upgrade, in which the VMM3a ASIC was developed [11]. It provides many different features for reading out MPGDs, that with the integration [12] of the VMM3a into the Scalable Readout System (SRS) [13] are made accessible also for applications outside of high energy physics. The SRS is a versatile multi-purpose readout system, developed by the RD51 collaboration [14] for the readout of MPGDs. It allows to read out small R&D set-ups as well as mid-sized experiments. For a more detailed description of the SRS, it is referred to [13,15].

The features of VMM3a/SRS include self-triggered readout channels, with a charge and thus energy sensitive analogue part, a MHz per channel rate capability, as well as an integrated hardware property called 'neighbouring-logic' (NL). While the self-triggered readout helps reading out large area detectors, the neighbouring-logic is of more general interest, because it allows recovering of more charge information in a self-triggered readout system (see Section 3.1 for a detailed description). Our goal is to explore these readout capabilities and to investigate the possibilities arising from the neighbouring-logic. From the point of view of possible applications, these features are of interest for digital X-ray imaging. Hence, we performed first studies on the imaging capabilities of this new system, using X-rays.

Starting with a description of the experimental set-up (Section 2), we present the main part of our work, which focuses on position resolution studies (Section 3). We show how segmented readout anodes introduce a modulation pattern in the position reconstruction and how the neighbouring-logic hardware feature of the VMM3a allows to mitigate this modulation effect (Section 3.1). Within this context, we also investigated if alternatives to the centre-of-gravity method should be considered to optimise the position reconstruction (Section 3.2). The goal for the neighbouring-logic is to show that it recovers otherwise lost charge information and thus allows a better position reconstruction, while the goal for the position reconstruction method is to understand if it is a smoothing effect and under which conditions it is applicable. For this, we performed simple modelling studies (Section 3.3), as well as spatial resolution measurements using the modulation transfer function and the edge spread function (Section 3.4). Afterwards, we present studies focusing on the energy resolution (Section 4). The goal is to show how the charge resolution of the VMM3a enables the option to perform energy-resolved imaging and especially how the neighbouring-logic will help to resolve interactions in the low energy domain. Within this context, we briefly illustrate how the rate capability of VMM3a/SRS can allow fast imaging.

2. Experimental methods

For the measurements, we used a COMPASS-like [8] triple-GEM [16] detector which was filled with a gas mixture of Ar/CO$_2$ (70/30%) at ambient pressure and temperature. The drift region is $3\,\mathrm{mm}$ wide, while the transfer gaps between the GEMs and the induction gap are $2\,\mathrm{mm}$ wide. The readout anode itself is highly segmented into 256 x- and 256 y-strips with $400\,\mathrm{\mu m}$ pitch. The top x-strips have a width of $80\,\mathrm{\mu m}$, while the bottom y-strips are $340\,\mathrm{\mu m}$ wide. This allows, by exploiting the charge sharing between the strips due to diffusion, a precise reconstruction of the incident particle's position.

Each channel of the readout electronics is connected to one anode strip. To match the standard 128 channel count per hybrid in the SRS, two VMM3a ASICs are wire-bonded on a Printed Circuit Board (PCB), the RD51 VMM-Hybrid V4.1, which is also equipped with an FPGA to set the parameters for the ASIC's operation [12]. One VMM3a has 64 readout channels, therefore a set of four hybrid PCBs was used to have the full detector read out and to obtain the charge information (10-bit ADC) [11] and time information (with nanosecond time resolution) [17] from each signal. It offers a continuous, self-triggered readout, with hit rates of up to $4\,\mathrm{MHz}$ per channel. Furthermore, the VMM3a combines several other properties, such as an integrated zero-suppression and neighbouring-logic [11].

Fig. 1. Sketch of the experimental set-up, with a photograph of the mammal, the entrance windows (EW), the line phantom (LP), the cathode (C), the drift (D), transfer (T$_i$) and induction gap (I), as well as the readout structure (RO).

As source for the X-rays we used a copper target X-ray tube (Ital Structures Compact 3K5 X-ray Generator) which emits X-rays mainly at $E_{\mathrm{K}_\alpha} = 8.0\,\mathrm{keV}$ and $E_{\mathrm{K}_\beta} = 8.9\,\mathrm{keV}$ [18]. The distance between the X-ray tube and detector was approximately $1\,\mathrm{m}$, ensuring uniform irradiation of the active detector area. For the measurements, we had either a line pair phantom fixed on the cathode or a small dead mammal positioned in front of the entrance window of the detector, as sketched in Fig. 1.

The studies have been performed without optimising the threshold level. The selection criterion was to have the signal rate significantly larger than the noise rate. This resulted in a threshold level of $70\,\mathrm{mV}$ above the baseline or approximately $10\,\%$ of the VMM3a's selected dynamic range. We accepted this high threshold level due to the detector gain of 10^4 at which the measurements were performed. The detector operation was reasonable, which is e.g. reflected in the quality of the X-ray spectra. This choice, which was not driven by the ASIC, should however not be considered as an absolute reference for future experiments.

3. Improvements in position resolution

An essential part for X-ray imaging applications is the reconstruction of the photon's incident position. Due to diffusion, the charge signal generated by an individual X-ray photon in the detector is spread over several readout channels, here anode strips. To find the corresponding charge clusters and reconstruct their position, we used a software-tool specifically designed for VMM3a/SRS data [19]. The signals from all activated channels are first sorted in time, which allows finding clusters in time: if subsequent signals have a time difference smaller than a certain value (in the present case $100\,\mathrm{ns}$) the signals are considered as a cluster in time. Next, these clusters in time are sorted in space, with signals on adjacent channels defined as a cluster in space, but allowing one missing channel in between. This is done for the signal on the x-strips and the y-strips independently. To have complete events with x and y coordinates, the independent clusters are matched by using the time information again, which means in our case that the clusters in each direction must have a time difference of less than $100\,\mathrm{ns}$ to be considered as an X-ray event. To determine the centre of the clusters x_c we used the centre-of-gravity (COG) method because it is simple, quick and intuitive:

$$x_\mathrm{c} = \frac{\sum_i Q_i x_i}{\sum_i Q_i} \ . \tag{1}$$

Here Q_i represents the measured charge on the strip x_i.

The COG method is a popular choice for the position reconstruction, however, when the distribution of the reconstructed cluster centres is plotted with high resolution (Fig. 2), a periodic pattern in the position data is observed. It is observed everywhere on the image but can be best understood in uniformly irradiated areas. A similar effect was already observed with Multi-Wire Proportional Chambers (MWPC) [20]. It is a result of a segmented readout electrode combined with threshold-based readout as illustrated in Fig. 3.

The charge, which is distributed over several readout strips, has to be digitised and further processed, with the condition that this takes
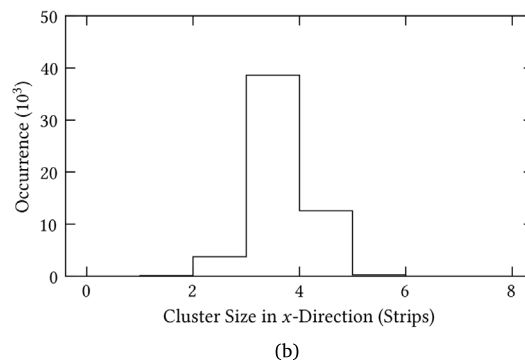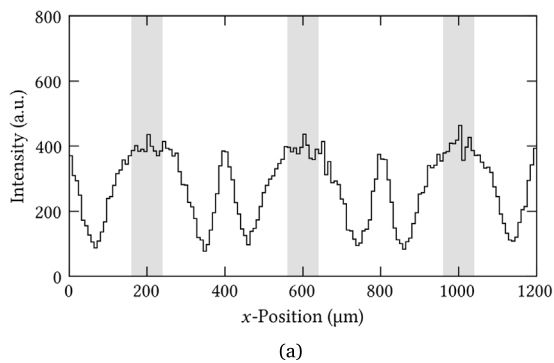
(a)

(b)

Fig. 2. In (a) the effect of the segmented readout on the reconstructed cluster position is illustrated. The histogram contains the x-coordinates of the reconstructed cluster centres. The vertical bars indicate the position and width of the readout strips. In (b) the corresponding cluster size distribution is shown, containing the number of x-strips per cluster.
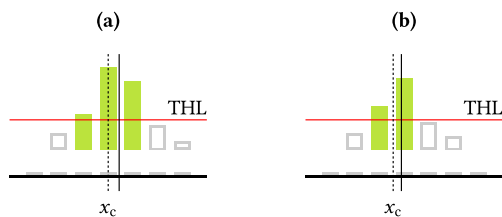

(a)

(b)

Fig. 3. Sketch of the origin of the repetitive pattern in the position data (Fig. 2). The charge distribution is represented by the vertical bars. The solid bars indicate the strips where the charge fraction is large enough to surpass the threshold level (THL). The vertical dashed lines indicate the reconstructed centre position x_c of the charge cluster, while the solid line indicates the actual cluster centre.

(a)

(b)

Fig. 4. Illustration of the working principle of the neighbouring-logic. In (a) the situation without NL enabled is shown. In (b) the effect of the NL is shown: even if the signal is too small to surpass the threshold level the neighbouring channels of a signal above threshold are read out as well.
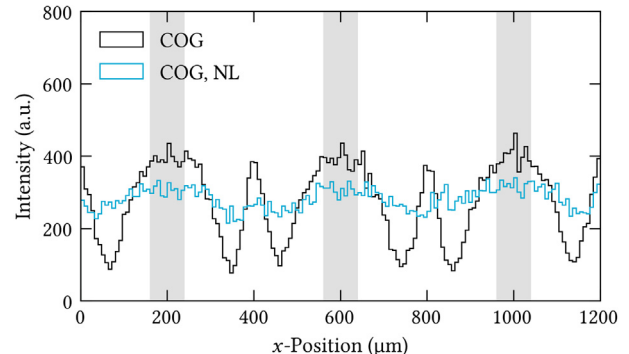
place, only if the signal on each channel surpasses a threshold level. Furthermore, the charge is integrated along each strip, because of the discretised readout anode. This has the consequence that information on the charge distribution of a cluster is lost when the centre position is determined. In case a signal on a channel surpasses the threshold level only slightly, the reconstructed cluster centre gets forced closer to the position of the central channel, if an odd number of adjacent channels have been triggered (Fig. 3a), while for the case of an even number of channels being triggered, the centre position of the cluster is likely located in between the two central channels (Fig. 3b). This leads to the peak structure, with one peak located at the strip position and the other one in between two strips. We should mention, that within our analysis an energy cut on the total cluster charge was applied. All events with a total cluster charge below 350 ADC counts are considered as noise. The cut value is illustrated later in this article (Fig. 6).

The observation of the modulation pattern in the position distribution indicates that the loss of charge information leads to an unsatisfactory accuracy in the position reconstruction. To mitigate the modulation effect, we focus on an integrated hardware property of the VMM3a, its neighbouring-logic (Section 3.1), as it allows to recover lost charge information. In addition to this hardware approach, we look at different position reconstruction methods to mitigate the modulation effect 3.2; we recall an established iterative detector response-based method (Section 3.2.1) and we present an event-based method where the charge in COG is weighted differently (Section 3.2.2). Afterwards, we model the effects of the neighbouring-logic and the weighting method with simple numerical calculations and Monte Carlo methods (Section 3.3) to get a first understanding under which conditions (threshold-level, charge cloud width, using a COMPASS-like strip readout), the charge weighting method is meaningful, also in combination with the neighbouring-logic. We continue with experimental studies (Section 3.4), using two methods to determine the spatial resolution of imaging systems: the modulation transfer function and the edge

Fig. 5. Comparison of the position distribution for the position reconstructed with the COG method and the NL enabled.

spread functions. As more charge information will inherently improve the position resolution, the goal for the VMM3a's NL is to validate experimentally that it recovers the charge correctly, while the goal for the charge weighting method is to understand, if it improves the spatial resolution or is a smoothing effect.

3.1. Hardware: VMM3a's neighbouring-logic (NL)

The Neighbouring-Logic (NL) of the VMM3a is implemented on a hardware level in the ASIC. Its working principle is illustrated in Fig. 4. When enabled, the two neighbouring channels next to a channel that surpasses the threshold level, are read out as well. This recovers charge information for the position reconstruction, and thus allows a more precise reconstruction of the cluster centre.
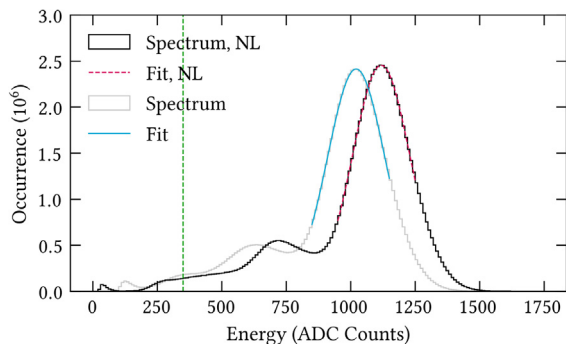
Fig. 6. Comparison of the energy spectra from the copper target X-ray tube, recorded with and without neighbouring-logic. Fitted to the peak is a single Gaussian function. The vertical dashed line indicates the position of an energy cut that we performed throughout the analysis. All events below the corresponding ADC value are considered as noise and discarded.

Fig. 7. Examples of the η-distributions for different cluster sizes.

Fig. 8. Correction distributions for two cluster sizes, derived from the η-distributions in Fig. 7 using Eq. (3).

The effect of the neighbouring-logic on the position distribution is shown in Fig. 5, where the distribution becomes more uniform, while its effect on the energy spectrum is shown in Fig. 6. Due to the additional charge recovered by the neighbouring-logic, the peak of the spectrum is shifted by about 100 ADC counts or 8.7 %. The measured energy resolution (FWHM) improves by enabling the NL from 25.5 % to 23.2 % at 8.0 keV. For more details on the NL's effects on the energy resolution, we refer to Section 4.

The recovering of charge information is particularly useful in the case of small signals, e.g. for Minimum Ionising Particles (MIPs) when using the μTPC method [21,22], both from the position reconstruction point-of-view as well as from the energy perspective. Furthermore, it allows to preserve a good detector performance in case of non-optimal signal-to-noise ratios; the threshold/discriminator level can be kept higher and in case of an otherwise lost signal, the tails can be still recovered. To completely contextualise the neighbouring-logic, it should be mentioned though, that the NL imposes a specific channel mapping on the detector, meaning that neighbouring readout strips/pads have to be connected to neighbouring channels of the VMM3a, which possibly discards the application in detectors with for example square pads or pixels. Also, the rate capability gets reduced, because more channels have to be read out than without NL. Hence, it is possible to turn it on and off, depending on the experimental needs. Something which was not explored in this work, is the noise rejection for the neighbouring channels. If needed, this can be done by utilising the time information signal's peak.

3.2. Data analysis: position reconstruction methods

The modulation effect shows that the COG method may not be the optimal choice to reconstruct the cluster position, in case charge information is lost due to the THL. An approach to mitigate this effect is to change the position reconstruction method. In the following, we recall the η-method, which is based on the detector response, also to examine the readout modulation from a different perspective. Afterwards, we present an empirical event-based approach, which we call the Q^2 weighting method, as we use the square of the charge as weight in the COG formula. This choice was specifically applied to a COMPASS-like triple-GEM detector and may not be adopted as a general solution.

3.2.1. Detector response-based correction: iterative η-method

An established approach to reduce the readout modulation is the η-method, which is described in detail in [23,24]. The idea is to correct each reconstructed cluster position with previously calculated correction distributions. To generate the correction distributions, the
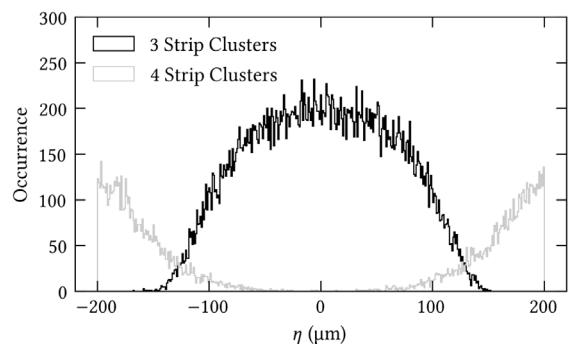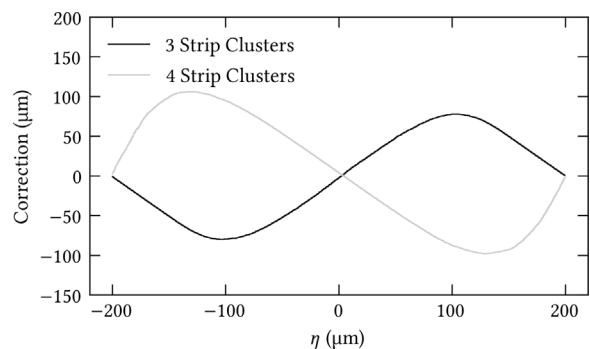
difference between the reconstructed cluster centre x_c and the centre of the closest adjacent strip s has to be calculated:

$$\eta = x_c - s . \tag{2}$$

The values of η are then histogrammed for each cluster size (Fig. 7). These histograms illustrate again the modulation effect, with odd strip count clusters reconstructed to the central strip of the cluster and the even strip count clusters being reconstructed in between two strips. From each histogram the expected number of entries $N_b^{\text{expected}} = N^{\text{tot}}/n$ for each bin b is calculated, using the total number of entries N^{tot} in the histogram and the number of bins n, assuming a uniform position distribution. From this, the difference between the measured entries per bin and the expected entries can be calculated for each bin: $\Delta_b = N_b - N_b^{\text{expected}}$. That allows to calculate the correction distribution for each binned value of η

$$\delta\eta_b = \frac{\sum_{i=1}^b \Delta_i}{N^{\text{tot}}} , \tag{3}$$

with examples for the correction distribution shown in Fig. 8. The correction is then performed on a bin level for each histogrammed position and each cluster size individually, meaning that the corrected position x_c' is given by $x_c' = x_c + \delta\eta_b$. The result of the corrected position distribution is shown in Fig. 9. Alternatively to the η-method, another iterative position correction method based on the pad response function [25,26] can be used; preliminary results show a similar behaviour as in Fig. 9, but further studies would be needed to properly quantify the effects.

3.2.2. Event-based correction: Q^2 weighting method

Instead of correcting the reconstructed position iteratively, the readout modulation can also be reduced by a different handling of the
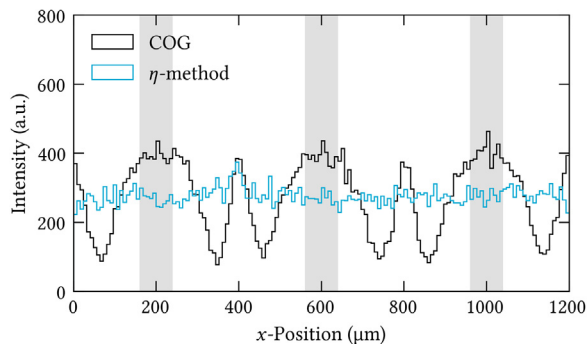
Fig. 9. Comparison of the position distributions obtained with the COG method and the corrected COG using the η-method.

Fig. 11. Illustration of the flat position response for Q^2 and NL combined, including a comparison of COG and NL.
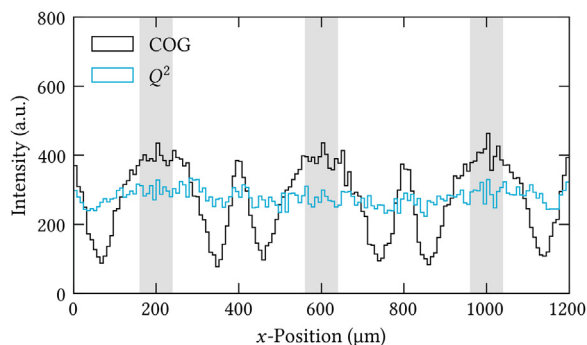

Fig. 10. Comparison of the position distribution, where the cluster centre was calculated with different algorithms. For the COG histogram via Eq. (1), while the Q^2 weighting histogram via Eq. (5).

Both, the position reconstruction with Q^2 and the neighbouring-logic, reduce the modulation pattern in the position distributions. The best effect can be obtained though by combining Q^2 with the NL, leading to a completely flat position response (Fig. 11). This effect is also illustrated in Fig. 12, where the same image is shown for the four reconstruction methods. Similar to the position distributions, the effect of the readout modulation is reduced and the intensity response becomes more uniform, which enables to recognise more details, e.g. the dot between the '1' and the '0'.

3.2.3. Excursus: results with MIPs

Having presented two methods (η and Q^2 weighting) that flatten the distributions of the reconstructed positions when using X-rays, we take a short excursus and apply them on a data set from a test beam tracker and compare them to COG. This allows us to get an indication if the same flattening seen with X-rays on the position distribution is observed with MIPs, here 150 GeV pions. Furthermore, the tracker data provide a reference point allowing to compare the position bias with COG and Q^2 quantitatively.

It is important to remark that the data, which have been recorded for the measurements presented in [29], were taken with APV25/SRS, the predecessor of VMM3a/SRS, which does not have the capability of a neighbouring-logic. The tracker uses the same detector type as we used for the X-ray studies, a COMPASS-like triple-GEM detector. In Fig. 13 the position distributions are shown. It can be seen that the position distribution becomes much more uniform, when the Q^2 weighting method is used, also with respect to the η-corrected position distribution. When calculating the residuals, giving access to the spatial resolution, it turns out that it improved from $\sigma_{\mathrm{COG}} = (47 \pm 1)\,\mu\mathrm{m}$ to $\sigma_{Q^2} = (42 \pm 1)\,\mu\mathrm{m}$, so by about 10 %, using the Q^2 weighting method, and that it gets worse when using the η-method: $\sigma_\eta = (54 \pm 1)\,\mu\mathrm{m}$. These numbers indicate that the Q^2 weighting method can improve the position resolution in COMPASS-like detectors.

3.3. Modelling the effects of NL and the Q^2 weighting method

We continue with simple Monte Carlo studies and numerical calculations, after introducing the neighbouring-logic and the Q^2 weighting method. The goal is to get a better understanding of their effect on the position reconstruction and to understand under which conditions (threshold level, charge cloud width) the Q^2 weighting method is meaningful, also in combination with the NL.

In our measurements, we used a two-dimensional x-y-strip readout, where the strips have a pitch of 400 µm. For the simulations, we simplified this readout structure to a one-dimensional readout with infinitely long strips. While the strip pitch remains the same in the simulation, we adjusted the strip width compared to our detector, as the charge in our simulation is collected geometrically. It means that the strips have not a width of 80 µm (x-strips) or 340 µm (y-strips), but a

available charge information, i.e. the change of the position determination algorithm; in [20] a method introduced by Georges Charpak et al. [27,28] was studied:

$$x_c = \frac{\sum_i (Q_i - B)\, x_i}{\sum_i (Q_i - B)} \ . \tag{4}$$

Here, B is a bias level that is subtracted from the measured charge. This gives less weight to the tails of the measured charge distribution or removes them completely, and gives more weight to the channels containing more charge information.

A complication of this method is the precise determination of an optimal bias value B. To give less weight to the tails and more to the channels with high charge values, we investigate an alternative approach that requires neither a pre-defined bias level nor the knowledge about the charge distribution, as it works on the event-by-event level. Instead of the charge Q_i we used the square of the charge as the weight for the position calculation:

$$x_c = \frac{\sum_i Q_i^2 x_i}{\sum_i Q_i^2} \ . \tag{5}$$

The result of this approach is shown in Fig. 10. The position distribution is more uniform, as expected for uniform irradiation.

It should be noted, that using Q_i^2 is an empirical relation to give less weight to the recorded tails of the charge distribution. A major goal of the studies in this article is to prove that in experimental conditions similar to ours, a different weight of the charge does not smooth the position distribution, but can improve the position response. The determination of the best value in the exponent, depending also on the readout geometry and the width of the charge cloud, should be investigated in future studies.
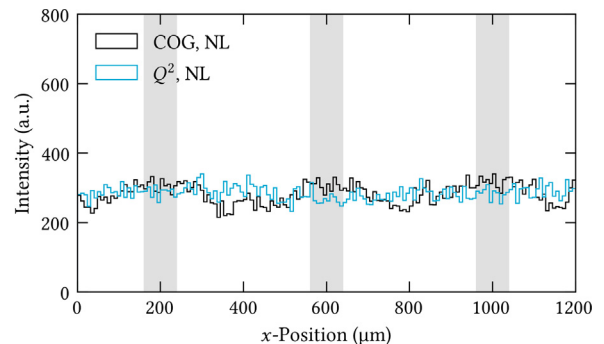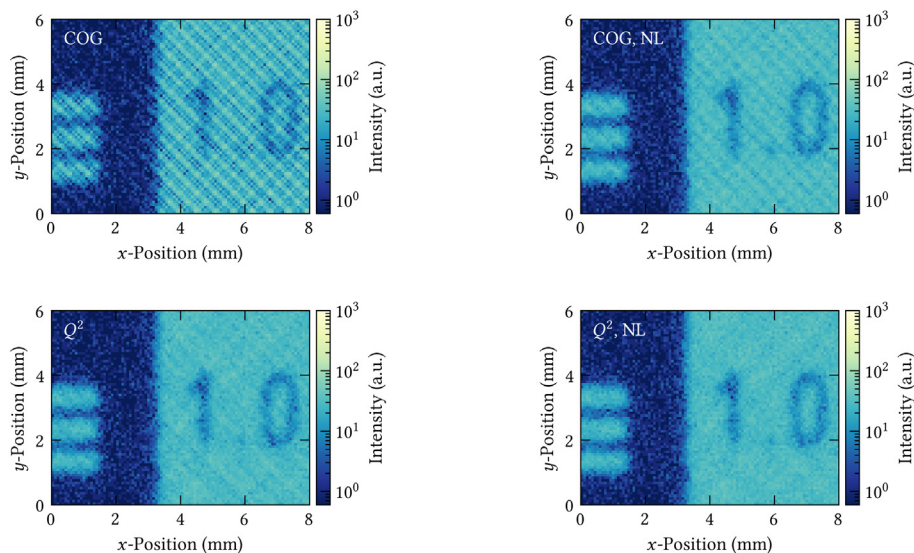
Fig. 12. Illustration of the effect of the readout modulation on a reconstructed X-ray image (section of the line phantom) for different reconstruction methods.
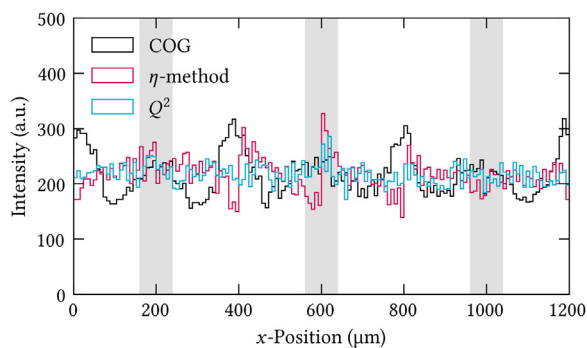

Fig. 13. Position distribution for the data from the test beam tracker. The neighbouring-logic was not available for these measurements, as they were performed with a different readout ASIC.

Fig. 14. Simulated position distributions for the different reconstruction methods and comparison with the initial position distribution.

width of $w = 240\,\mu m$. This effective strip width arises from a measured $60/40\%$ signal sharing between the x and y-strips in our detector and corresponds to the width the x-strips would need to have if the charge would be collected only geometrically. Our goal was to stay close to our experimental set-up, meaning that we did not change the dimensions of the readout structure for the presented modelling.

To calculate the charge Q_i on each strip i, we used a two-dimensional Gaussian distribution that represents the charge distribution:

$$Q_i = \frac{1}{2\pi\sigma_x\sigma_y} \int_{s_i-\frac{w}{2}}^{s_i+\frac{w}{2}} \int_{-\infty}^{\infty} e^{-[(x-\mu_x)^2/\sigma_x^2+(y-\mu_y)^2/\sigma_y^2]/2} \,\mathrm{d}y\,\mathrm{d}x$$

$$= \frac{1}{\sqrt{2\pi\sigma_x^2}} \int_{s_i-\frac{w}{2}}^{s_i+\frac{w}{2}} e^{-(x-\mu_x)^2/(2\sigma_x^2)} \,\mathrm{d}x \; .$$

(6)

Here μ corresponds to the centre of the charge distribution, σ to its width, s_i to the centre position of the strip i.

First, we want to reproduce our observations of the readout modulation. Therefore, we had to identify the width σ_x of the charge distribution and the threshold-level, as they define the cluster size. We measured an average X-ray cluster size of 3.1 strips with a threshold level of around 10% of the VMM3a's dynamic range. Thus, we introduced in the simulation a corresponding threshold level and varied
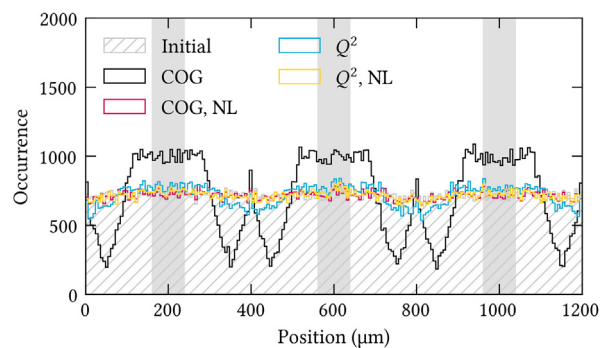
σ_x until we reached the same value for the cluster size. The result is $\sigma_x = 320\,\mu m$. Knowing the charge collected on each strip Q_i as well as the threshold level, the neighbouring-logic can be introduced and the central position of the cluster can be calculated with the same methods as in our actual analysis. The resulting position distribution is shown in Fig. 14. Even though it is not perfectly reproducing the position distribution from the experimental data (due to the approximations done in the modelling), we consider the reproduction of the data as sufficiently good for our purpose.

Included in the simulation are Monte Carlo methods, to sample the initial cluster position from a uniform distribution, allowing to calculate the displacement $\delta = x_{\mathrm{ini}} - x_{\mathrm{rec}}$ of the reconstructed cluster position x_{rec} from the initial actual cluster centre x_{ini}. The result is shown in Fig. 15. We also sampled values from an exponential distribution $f(l) \propto \exp(-l/\lambda)$ [30] to describe the intensity loss of an X-ray beam in a medium, with l the interaction depth. This is done to get a hand on different drift lengths, which leads to a variation of the diffusion and thus different cluster sizes. The results of this are the two structures with a different slope for each reconstruction method, shown in the inset of Fig. 15. The attenuation length $\lambda = (\alpha\rho)^{-1} = 6.8\,\mathrm{cm}$ [30] in Ar/CO_2 $(70/30\%)$ at Normal Temperature and Pressure (NTP) of $8.0\,\mathrm{keV}$ photons is calculated with the mass absorption coefficient $\alpha = 85.5\,\mathrm{cm^2/g}$ [31] and the material density $\rho = 1.716\,\mathrm{g/L}$ [32]. To deal with variable drift lengths it is necessary to
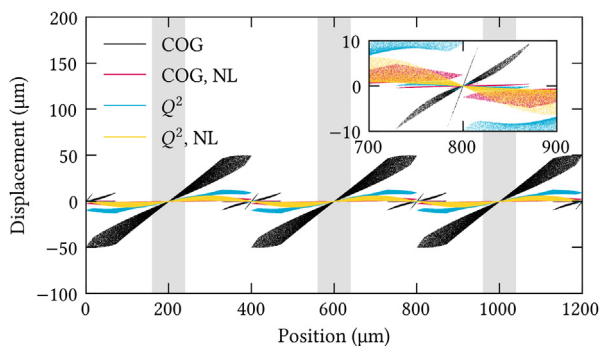
Fig. 15. Displacement between the reconstructed cluster position and the initial cluster position for the four different position reconstruction methods.
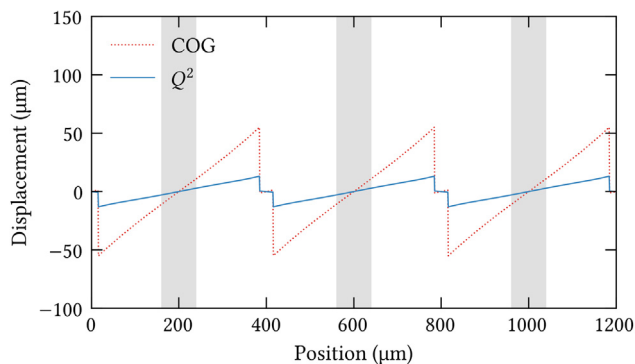

Fig. 16. Example of the displacement of the reconstructed position depending on the initial position for COG and Q^2 ($\sigma_x = 320\,\mu m$ and THL = 5 %).

(a)

(b)

Fig. 17. Plot (a) shows the mean residuals between the reconstructed and the initial position for different threshold levels. Plot (b) shows the average Cluster Size (CS), the most probable CS, and the CS variation for different threshold levels ($\sigma_x = 320\,\mu m$).

calculate the diffusion coefficient D_T instead of using the mean width σ_x of the charge distribution. Because we know the mean width of the charge distribution, we can define D_T by the difference between the maximum drift length $L_{max} = 9\,mm$ and the mean interaction depth of the X-ray photons:

$$\sigma_x = D_T \sqrt{L_{max} - \langle l_{int} \rangle} \,, \tag{7}$$

where $\langle l_{int} \rangle$ for a 3 mm wide drift region is given by

$$\langle l_{int} \rangle = \int_{0\,cm}^{0.3\,cm} l \times \frac{e^{-l/\lambda}}{n} \, dl = 0.149\,cm \,, \tag{8}$$
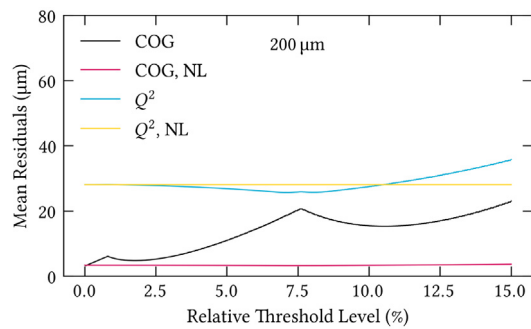
with n the normalisation constant. The resulting diffusion coefficient $D_T^{sim} = 369\,\mu m/\sqrt{cm}$ is larger than the one expected from calculations with Magboltz [33], $D_T^{mag} = 239\,\mu m/\sqrt{cm}$. This is because the cluster size is not only influenced by the diffusion, but also by the track length of the photoelectron, which in Ar/CO_2 (70/30%) at NTP is about 500 μm for 8.0 keV photons [25]

The simulation shows the significant impact of the neighbouring-logic on the position reconstruction, but it also suggests that there may be situations, where the Q^2 weighting method, when combined with the neighbouring-logic, results in the best position reconstruction. Being able to reproduce the modulation effect, the goal in the following is to get an insight, under which conditions (threshold level, charge cloud width) the Q^2 weighting method can be applied and to find possible limitations of it.

The charge per strip in Eq. (6) results in a normalised total charge of 1. In the following calculations, we could adjust two parameters: the width of the charge cloud σ_x (now simplified, without different interaction depths) and the threshold level. The latter will be here given in fractions of the total charge. We calculated again the displacement δ between the reconstructed cluster position and the actual cluster centre (see Fig. 16 as an example). In Fig. 17a an example for the plot of
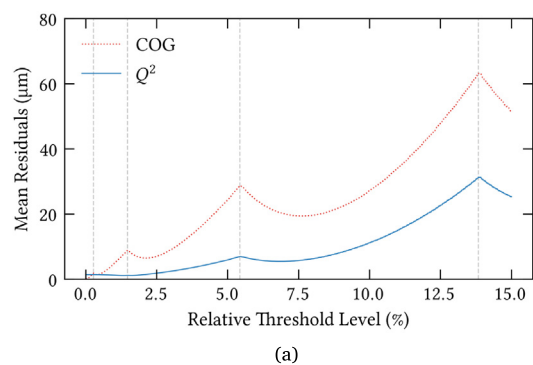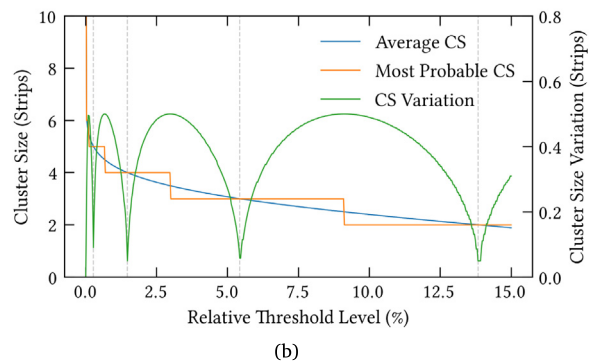
the mean of the absolute value of the residuals δ is plotted against the threshold. There, Q^2 leads to better-reconstructed positions than COG, except for threshold values of THL < 1 %.
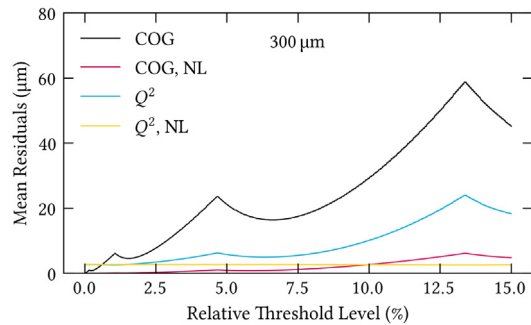
The peaks that are observed are related to the cluster size and its variation, as illustrated in Fig. 17b. The peaks appear, when the cluster size variation is the smallest; a barely varying cluster size means that the reconstructed cluster position will be forced at the central strip (for an odd number of active channels) or in between the two central ones (for an even number of active channels, which in other words means that the effect of the readout modulation is maximal. This peak behaviour is likely to be a result of the simplified calculation because it does not include signal variations due to noise, different drift lengths or different energies deposited in the detector. However, because the general trend of the lines and the relative variation is preserved, we accepted this kind of behaviour.

Calculations as for Fig. 17a have been performed for various charge cloud widths, of which the results are shown in Fig. 18. It can be seen that the neighbouring-logic always improves the position reconstruction. In case the charge cloud width is not significantly smaller than the strip pitch, the Q^2 method gives better results than the COG, also with neighbouring-logic enabled.
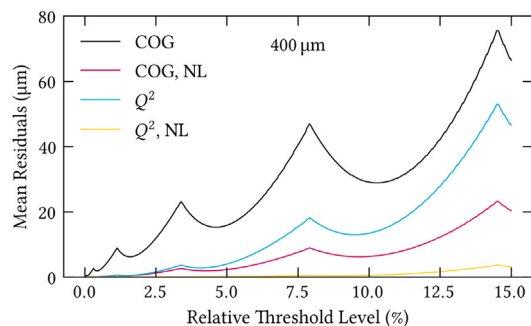
Some of the data sets illustrated in Fig. 18 show an almost threshold independent response of the displacement. This has been studied, by generating the position distributions (similar to Fig. 14) for several charge cloud widths, of which two extreme examples (for illustration purposes) are shown in Fig. 19. Even though the average cluster size is still of the order of 3 to 4 strips, the charge cloud width is small (in the given example $\sigma_x = 150\,\mu m$) with respect to the strip pitch ($p = 400\,\mu m$), meaning that a lot of charge is located in one channel. With this, the COG forces the position to be around this strip, which is an effect that gets enhanced when using Q^2. At this moment, when a considerable
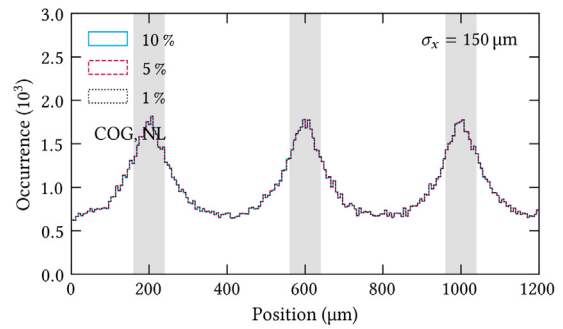
(a)

(b)

(c)

Fig. 18. Results of the displacement calculations for the four position reconstruction methods, using three different charge cloud widths ($\sigma_x = [200, 300, 400]\,\mu\text{m}$).
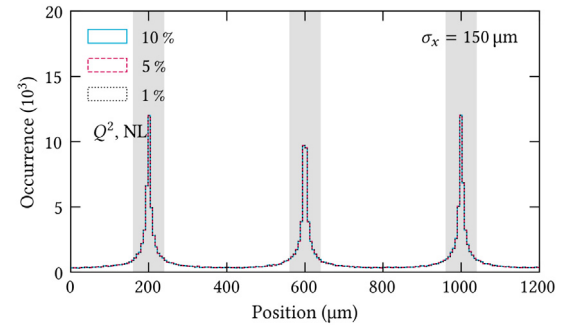

(a) COG, NL

(b) Q^2, NL

Fig. 19. Examples of the position distribution at very small charge cloud widths ($\sigma_x = 150\,\mu\text{m}$) for different threshold levels, using the COG method (a) and the Q^2 weighting method (b). In both cases the neighbouring-logic was included in the calculations.

3.4. Spatial resolution measurements

The position distributions and the simple models show that the neighbouring-logic improves the spatial resolution and that the Q^2 weighting method can reduce the deviation in the position reconstruction introduced by the modulation effect in certain conditions. Our goal is now to investigate this from an experimental point of view, to confirm that the NL recovers the lost charge information and that the Q^2 weighting method is not a smoothing effect in experimental conditions like ours. For this, we used two different methods to determine the spatial resolution: the Modulation Transfer Function (MTF) and the Edge Spread Function (ESF), which will be introduced in the following.

3.4.1. Modulation transfer function (MTF)

To determine the modulation transfer function, a line phantom made of $50\,\mu\text{m}$ thick lead with slits of varying widths is used. Each group of slits represents a specific spatial frequency f, given in line pairs per millimetre (LP/mm) [34]. The obtained X-ray image of the phantom is shown in Fig. 20.

To get information about the imaging capabilities of a system, the contrast c, which is defined as the intensity ratio between the open areas (slits) and the covered areas [35], is used:

$$c = \frac{I_{\max} - I_{\min}}{I_{\max} + I_{\min}} . \tag{9}$$

Here $I_{\max}$ is the mean out of three intensity maxima and $I_{\min}$ is the mean out of two intensity minima, for each spatial frequency.

To get these values, a transmission profile as shown in Fig. 21 has to be generated. For this, we used the projection of all cluster centres, within the dotted areas (see Fig. 20), on the y-axis. Because of the projection, the intensity in our plots corresponds to cluster counts N per bin. From this counting, we derive that the error on the intensity

amount of 'correct charge information' is available, but mainly on one channel, Q^2 starts to 'over-correct' the channel that otherwise would be considered as best, because it contains the highest charge information. From that, the position distribution becomes almost threshold independent, explaining the observations, especially from Fig. 18a.

Despite the peak structure observed e.g. in Fig. 17, which is a consequence of the simplified model, these calculations allow to get a principle qualitative understanding under which conditions the Q^2 method improves the accuracy of the reconstructed position. For our calculations, we stayed close to our experimental set-up, which is one specific situation. Future studies may focus on adjusting the simple calculation set-up to other readout structures (e.g. rectangular or hexagonal pad) or other geometrical parameters of the strip readout. This would allow to get a coarse insight on geometrical effects on the position reconstruction with the Q^2 weighting method, e.g the effect of the strip width-to-pitch ratio.
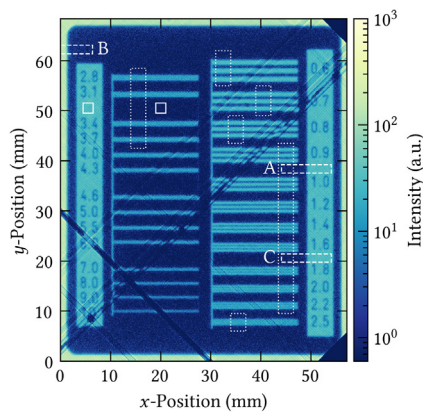
Fig. 20. X-ray image of the line phantom (the positions were reconstructed with the COG method and NL enabled). The solid and dotted lined rectangles indicate the areas which have been used to determine the spatial resolution via the MTF, while the dashed lined rectangles with the labels A, B and C indicate the regions for the ESF measurements. The readout strips are not aligned with the phantom features, as it can be seen by the diagonal lines originating from dead or masked channels and strips.

maxima and minima is given by $\sqrt{N}$. The selection of the areas was necessary due to dead or noisy (and thus masked) strips and channels in our set-up (diagonal lines in Fig. 20). These lines are diagonal because the MTF phantom was tilted by 45.1° with respect to the readout strips. The reason behind this are Moiré patterns that are unavoidable when using a 2D grid readout and a line phantom. To get the best average and give no preference to one readout direction, we tilted the MTF phantom by 45°.

With larger spatial frequency, the contrast decreases. This allows finding the smallest structure size which can still be resolved. However, the contrast obtained with Eq. (9) needs to be normalised by the maximum possible contrast c_{max}, so the contrast between a fully open and a fully covered area (solid lined areas in Fig. 20). This gives the value of the MTF for each spatial frequency:

$$\text{MTF}(f) = \frac{c(f)}{c_{max}} \ . \tag{10}$$

The results are shown in Fig. 22. To get a value for the spatial resolution of the imaging system, often the inverse of the spatial frequency at the 10 %-level of the MTF is used [34]

$$r_{\text{MTF}} = f^{-1}\big|_{\text{MTF}=10\%} \ , \tag{11}$$

which in the shown example results in $r \approx 400\,\mu\text{m}$.

Due to its transmission profile, the MTF give access to the imaging capabilities of a system, even without a quantitative expression for
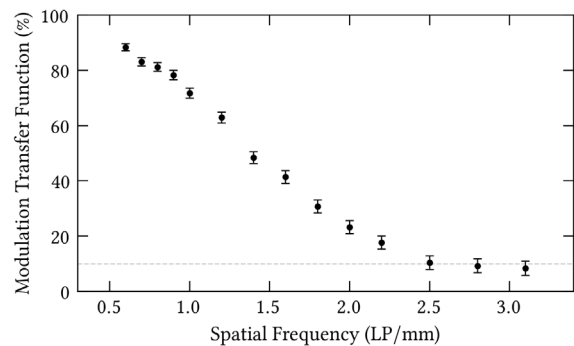

Fig. 22. Modulation transfer function, which was obtained from the data shown in Fig. 21 (COG, NL). The horizontal dashed line indicates the 10 %-level of the MTF.
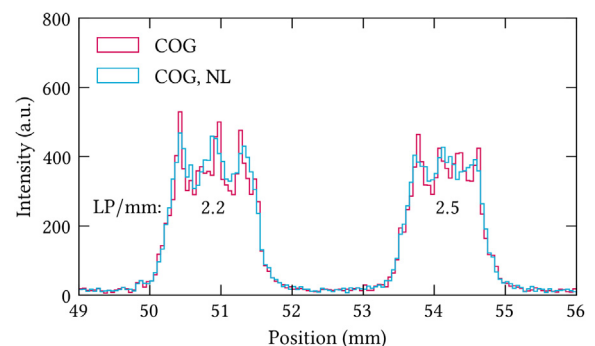

Fig. 23. Comparison of the transmission profiles. At 2.5 LP/mm four intensity maxima can be observed for the COG case, although the mask has only three slits at this spatial frequency. When using COG with NL or Q^2, the fourth 'fake' peak disappears. We did not show Q^2 to keep a clear plot, but it looks similar to COG with NL.

the spatial resolution, as illustrated in Fig. 23. There two transmission profiles for the COG method (with and without NL) are shown. It can be observed that the transmission profile at 2.5 LP/mm, shows four intensity maxima for COG, although the MTF mask has only three slits at this position. This is likely to be caused by the readout modulation. When the neighbouring-logic is used, so when the readout modulation is significantly smaller, the 'fake' peak disappears.

Another observation in Fig. 24 is likely to be explained with the same underlying effect of the readout modulation that causes the fourth peak. It can be seen that the difference between intensity minima and
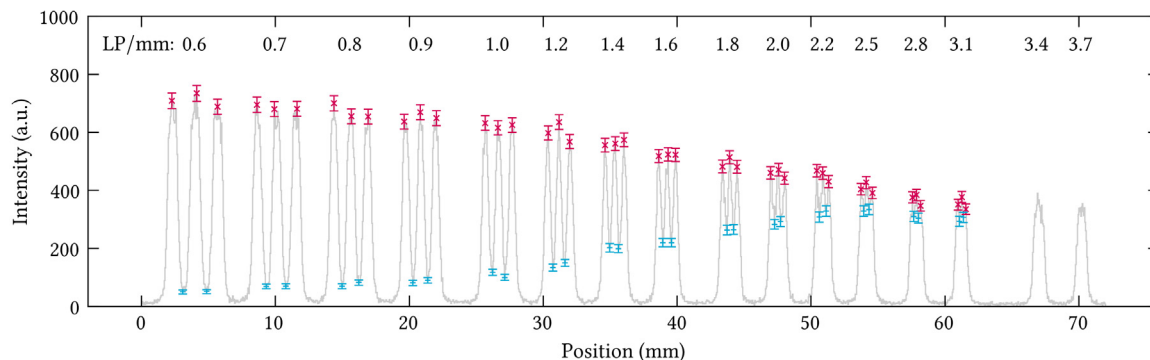

Fig. 21. Transmission profile obtained from the X-ray image of the phantom, using COG with NL enabled. The points indicate the intensity maxima (×) and minima (+), while the number above each group of peaks indicates the spatial frequency of this group. The error bars correspond to a $\sqrt{N}$-error. For the sake of completeness, the transmission profile at 3.4 LP/mm and 3.7 LP/mm is shown, although it is not used for calculating the MTF.
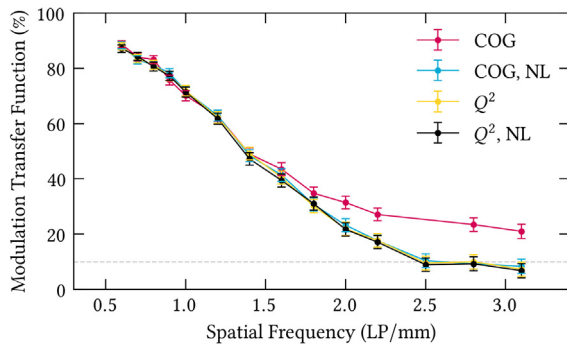
Fig. 24. MTF Comparison for the four reconstruction methods.

Fig. 26. Plot of the projection on the long axis of the data shown in Fig. 25 (region A), reconstructed with COG and NL. The error bars correspond to a $\sqrt{N}$-error. Fitted to the data is Eq. (12).
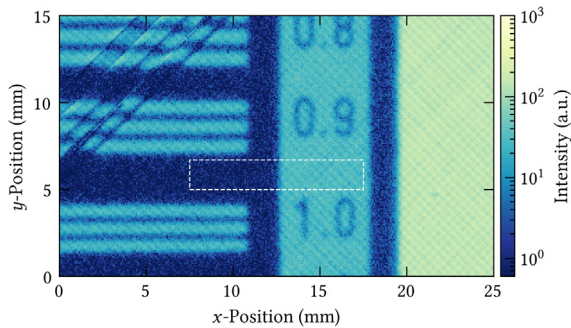

Fig. 25. One of the edges of the mask (region A), which was used for the resolution measurements via the ESF. The data within the rectangle are projected along the long axis and then histogrammed for the ESF fit (Fig. 26). For the position reconstruction of this image COG with NL was used.

Table 1
Spatial resolution obtained via the ESF from the integrated intensity distribution for three different regions.

Method	σ_A (µm)	σ_B (µm)	σ_C (µm)
COG	172 ± 10	180 ± 13	194 ± 17
COG, NL	170 ± 8	181 ± 5	193 ± 10
Q^2	169 ± 9	180 ± 6	190 ± 10
Q^2, NL	164 ± 9	182 ± 5	189 ± 10
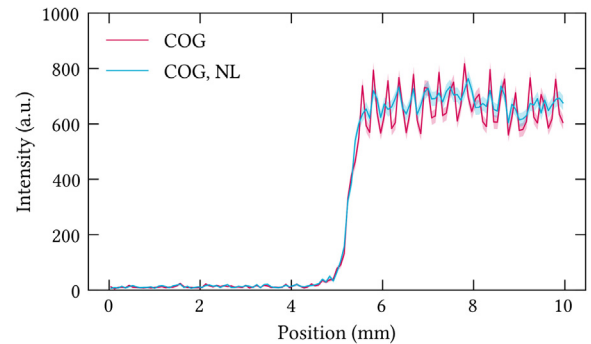
Fig. 27. Example for the comparison of the ESF data (region C), for the cases with and without NL, using the COG method. The data points are connected with a line and the error bars are represented by the shaded band. Here a rougher binning than for the position distributions was used (1 bin ≡ 80 µm). The average distance d between the spikes is 280 µm, which is expected for a structure with two peaks per 400 µm but that is tilted by 45°: $d = \sqrt{2} \times 400 \,\mu m/2 = 283 \,\mu m$.

maxima for COG is larger than with NL enabled. From Fig. 2, for example, a strong intensity variation for COG is observed, which is an artefact of the readout modulation. However, because the contrast is calculated from the intensity, the value of the contrast gets larger, if the artefacts of the intensity variations caused by the readout modulation are included. It is not avoidable to exclude this effect, because it is part of the position reconstruction with COG. This results in an over-enhancement of the calculated contrast for the COG method. This explains why the MTF for COG in Fig. 24 seems to be better at higher spatial frequencies than the other three methods, although it is not, as illustrated with Fig. 23. To our regret, the uncertainties on the MTF data points do not reflect these systematic artefacts caused by the readout modulation.

For the other three methods (the transmission profile for Q^2 and Q^2 with NL looks similar to the one shown for COG with NL), the three intensity maxima are reconstructed correctly and the results are compatible with each other.

3.4.2. Edge spread function (ESF)

The ESF is based on resolving a sharp edge, i.e. the transition between a completely covered and an irradiated area. In the ideal scenario, the transition is only affected by diffraction, leading to an almost step-like transition. In practice, this steep transition gets smeared out because of the drift and diffusion of the ionisation electrons and the track length of the photoelectron, which is liberated by the incident X-rays [36].

The phantom has sharp edges, which we use for the ESF. One of the selected regions is shown in more detail in Fig. 25. The data are then projected on one axis and fitted with the following expression (Fig. 26),
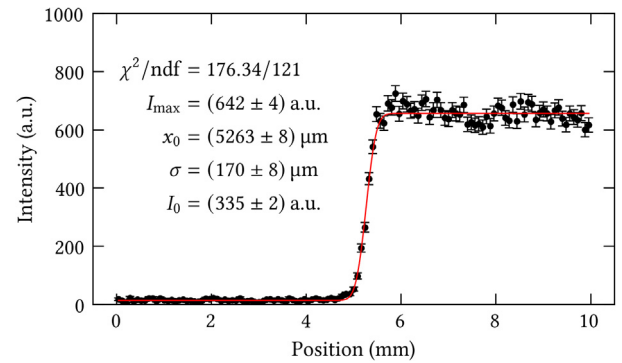
based on the Gaussian error function:

$$I(x) = \frac{I_{max}}{2} \mathrm{erf}\left(\frac{x - x_0}{\sqrt{2}\sigma}\right) + I_0 . \tag{12}$$

Here I_{max} is the maximum intensity, I_0 corresponds to the baseline intensity, x_0 is the position of the edge and σ is the width of the edge, which corresponds to the spatial resolution determined with this method. In the given example $\sigma = (170 \pm 8)\,\mu m$ is obtained. This value corresponds to a FWHM of $\sigma \times 2.355 = 400\,\mu m$, which is compatible with the result obtained with the MTF at 10 %, as expected [37].

The ESF studies were performed for the three regions A, B and C (Fig. 20), with the obtained results for the spatial resolution being listed in Table 1. Within the uncertainties, all values are compatible with each other. The largest uncertainty is seen for COG. This is likely to be caused by the readout modulation, as illustrated in Fig. 27. There, the ESF is compared for COG and COG with NL enabled. The intensity
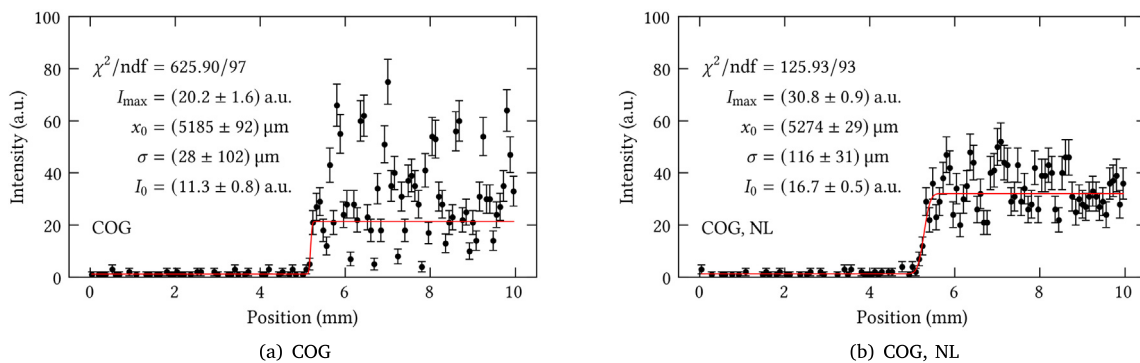
(a) COG

(b) COG, NL

Fig. 28. Comparison of the ESF plots from the slices of the scan. Here the 10th slice from region C, so $y \in [764, 849]\,\mu m$, was selected.
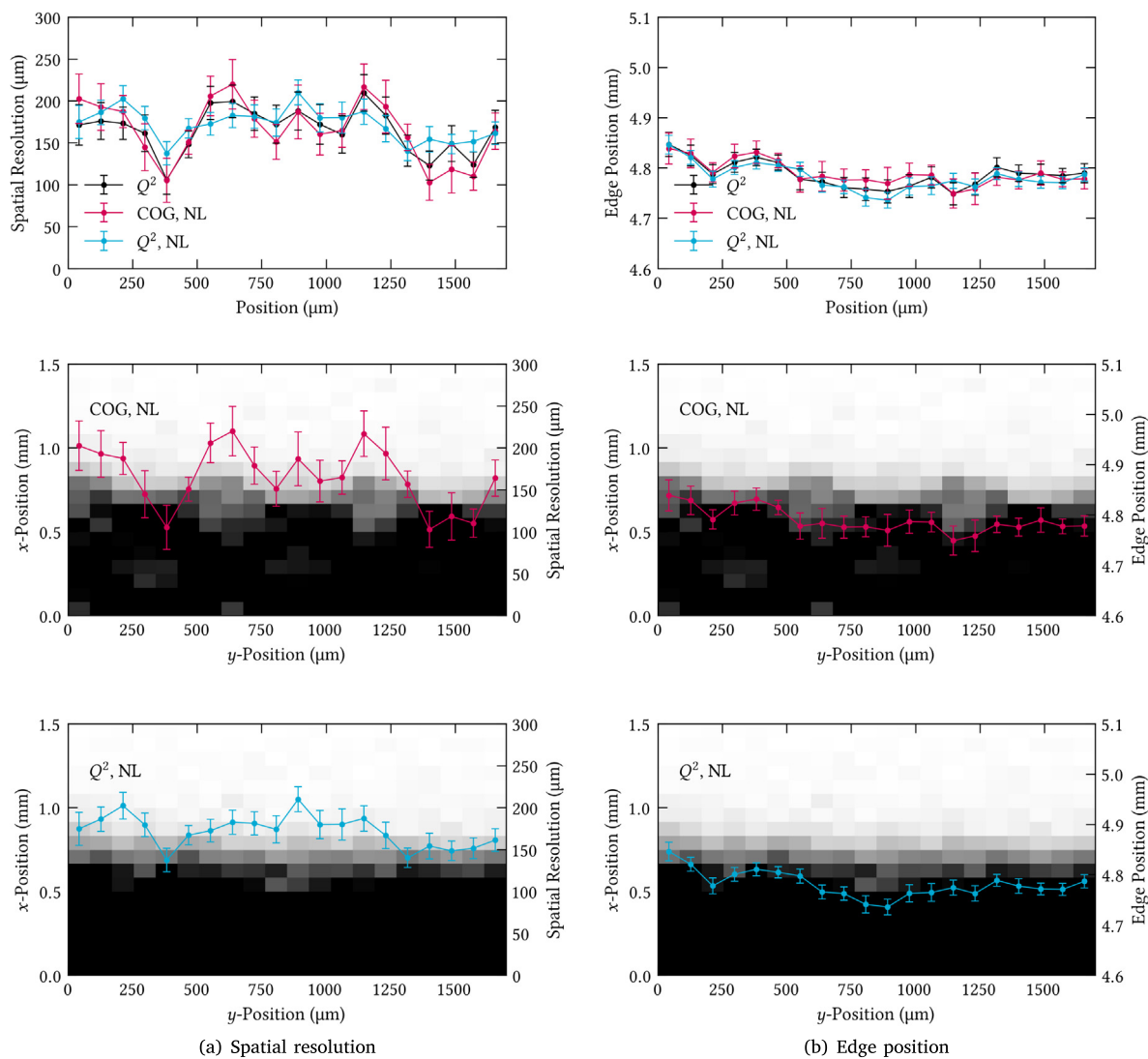

(a) Spatial resolution

(b) Edge position

Fig. 29. The top row shows the comparison of the spatial resolution (a) and the mean ESF position (b) for different reconstruction methods, depending on the position along the sharp edge from region B. The middle row shows images of the sharp edge in region B (rotated by 90° with respect to Fig. 20), with the overlay of the spatial resolution (a) and the mean ESF position (b), which have been reconstructed with the COG method and NL enabled. Here, a higher brightness of the bin/pixel means lower intensity/counts. In the bottom row the overlay of the sharp edge with the spatial resolution and the mean edge position is shown, but reconstructed with Q^2 and NL.
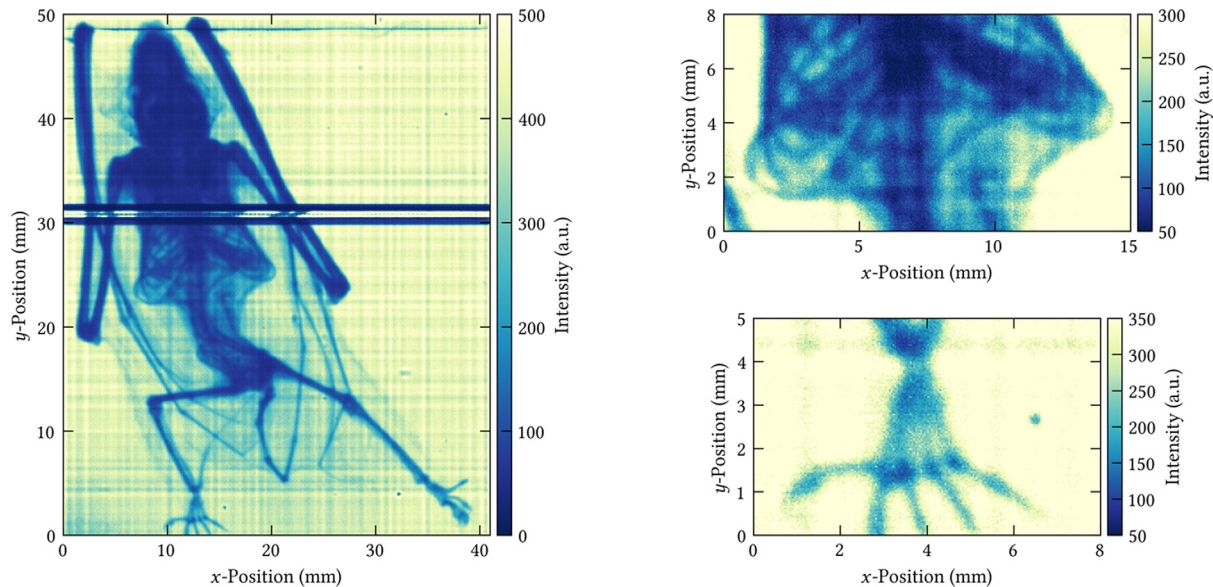
Fig. 30. Left: X-ray image of a bat, recorded within $35\,\mathrm{min}$ and containing 421×10^6 clusters. For the position reconstruction we used the combination of NL and Q^2. Top right: image of the bat's torso, with more than 14×10^6 clusters. Bottom right: image of the bat's claw, with more than 8.5×10^6 clusters.

plateau has larger fluctuations for COG, which is similar to the effect that was already observed for the MTF comparison in Fig. 23.

Because the readout modulation has a significant impact on the position reconstruction, the strong modulation effect observed in Fig. 27 raises the question, why the values for the spatial resolution in Table 1 are so similar for the different methods? It can be a consequence of integrating many clusters in each region A, B and C for the ESF fit, resulting in a fit that gives only access to the *average* resolution, and that is not sensitive any more to accuracy effects on the position reconstruction by the modulation effect.

To investigate, if the similarity of the resolution values is caused by the integration, and to get a deeper insight into the modulation effect's impact on the spatial resolution, we studied each ESF region locally by slicing each region into 20 equal-sized parts and performing the ESF study for every slice. Two examples for the ESF slice studies are shown in Fig. 28. It illustrates that on a local level the measured intensity behaviour is affected substantially by the readout modulation. This means that a uniform intensity response is not observed, especially for the case where only COG is used. This is additionally confirmed by the numerical values for the goodness of the fit (χ^2/ndf), which also shows that for the other cases, here exemplary COG with NL, a fit is still reasonable. Hence, we continued our resolution studies without COG. Examples of their outcome are shown in Fig. 29, where the spatial resolution σ and edge position x_0 of each ESF fit are plotted against the slice position. In both cases, for the resolution and the position, a wave behaviour is observed. For the position, this behaviour does not seem to be affected by the reconstruction method, while for the spatial resolution it seems to get reduced when using Q^2 (with NL) instead of COG with NL. In fact, it can be seen by overlaying the resolution for each slice with the image of the sharp edge, that the wave behaviour of the spatial resolution is following a wave behaviour introduced by the readout modulation. When using Q^2 with NL, the readout modulation on the sharp edge is less visible and the resolution is less affected by it. These results indicate that the data in Table 1 are affected by an averaging effect.

We conclude from the MTF and ESF studies, that the neighbouring-logic is a useful feature to improve the position reconstruction with the VMM3a. We also conclude that the Q^2 weighting method, which gives compatible results with COG having NL enabled, is not per se a smoothing effect where information gets lost. In our case (soft X-rays, NTP, and COMPASS-like triple-GEM detector), it helps to improve the spatial resolution and increase the accuracy of the position and resolution response, especially when it is combined with the neighbouring-logic.

4. Improvements in energy resolution

In the following section, we present the neighbouring-logic's effect on the energy resolution. Improvements in the low energy regime are shown (in case a wide dynamic range has to be used), as well as the preservation of a reasonable detector performance in unfavourable signal-to-threshold ratios. First though, we give a minor prospect on fast imaging with VMM3a/SRS.

The high-rate readout capability of VMM3a/SRS allows to acquire images with a large number of clusters in a shorter time. As an example, we show the X-ray image of a bat (Fig. 30). This image contains more than 421×10^6 clusters, which have been acquired within $35\,\mathrm{min}$. This corresponds to an interaction rate of $200\,\mathrm{kHz}$ in the selected area or to a hit rate of up to $20\,\mathrm{kHz}$ per channel. These numbers are far below the limits of VMM3a and SRS and ongoing developments in the DAQ chain will allow moving this rate further, approaching the intrinsic capabilities of MHz per channel. With a large number of recorded interactions, it is also possible to identify structures, which otherwise are difficult to resolve. For this, we would like to point out the body parts of the bat, specifically the bone structure of the torso and claw, which can be clearly resolved.

Due to the noise level in the experimental setup, the measurement was performed with a relatively high but still reasonable THL (around $14\,\%$ of the selected dynamic range). This allows us to point out again one of the advantages of the neighbouring-logic: preserving a reasonable detector performance in experimental situations with a non-optimal signal-to-threshold ratio. This is illustrated in Fig. 31. There, the X-ray image of the bat is shown for the case without NL and for the case with NL enabled. For the case of COG, a strong effect of the readout modulation can be observed. It should be noted that this is an extreme scenario. With the neighbouring-logic, the influence of the high threshold level gets significantly reduced, resulting in a reduction of the modulation effect and an improved image of the bat. The modulation effect, which can be observed with COG, gets significantly reduced.

With the VMM3a's ADC, energy-resolved imaging studies by selecting specific energy ranges can be performed. To illustrate this, we used a cut from Fig. 30. The energy spectrum of the events in the specified region is shown in Fig. 32. We selected the events from three regions of the spectrum, the low energy region, the photopeak region and the Bremsstrahlung region. From these events, we generated the images shown in Fig. 33. The entries per bin/pixel in each image have been
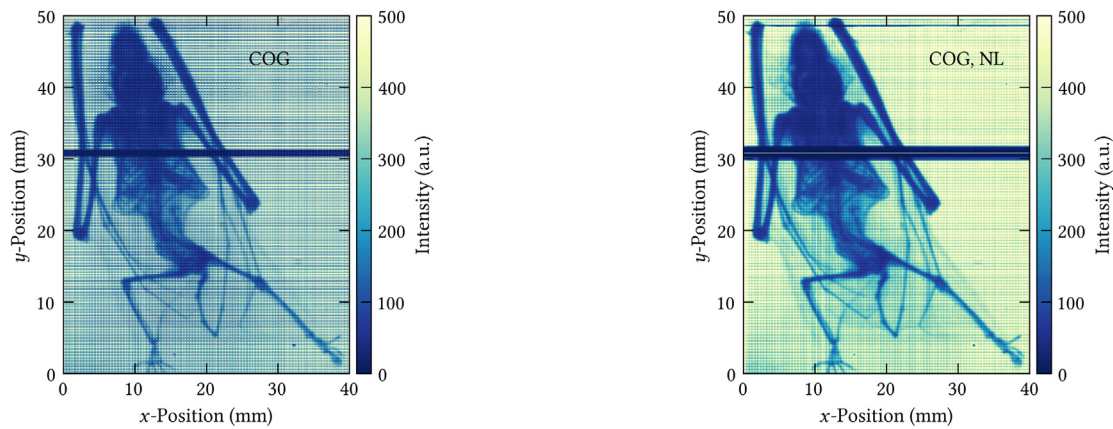
Fig. 31. Comparison of the X-ray image of the bat, where the position has been reconstructed with COG and with COG and NL enabled.
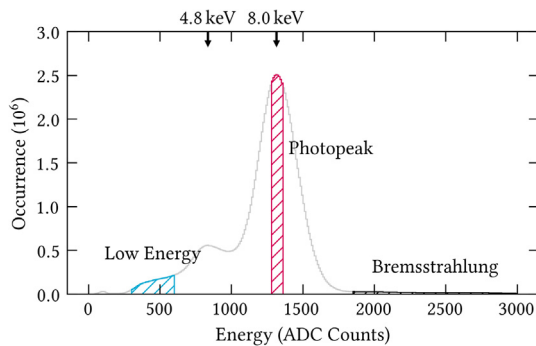

Fig. 32. Energy spectrum, showing the energy regions that we used for the energy-resolved images of the bat. The annotated energy values are the expected ones and have not been calibrated, but the ratio of the corresponding ADC values and the ratio of the annotated values are compatible within 10%.

normalised to the total number of entries in each selected region, to get comparable intensity values.

In these images, the effect of different cross sections of the interaction of the photons with matter can be seen. The resulting absorption depends highly on the photon's energy and the density of the material. The photon energy in the Bremsstrahlung region for example is so high that most of the photons are passing through the bat, resulting in an almost uniform intensity response, independent of the tissue's density.

In addition to the energy selection, we would like to highlight the advantages that the neighbouring-logic can provide to resolve interactions where small amounts of energy are deposited in the detector and a wide dynamic range has to be used, a situation typical for e.g. fluorescence imaging. The events with low energy deposition that we use for this purpose are fluorescence X-rays that are emitted by the argon atoms (after the photoelectric ionisation of the atoms by the primary X-rays) and that do not escape the active detection volume but interact within the detector. A description of the event identification via the nanosecond time resolution of the VMM3a can be found in a previous work [38]. This work is also the source for the data, which are presented in the following. There we could operate at a lower threshold (around 5% of the selected dynamic range) than for the other measurements presented in this article.

As one of the conditions for this study is to keep a large dynamic range, this measurement allows also to compare the effect of the neighbouring-logic on the measured energy resolution in situations with a high signal-to-threshold ratio (photopeak at $8.0\,\mathrm{keV}$) and a weaker signal-to-threshold ratio (argon fluorescence line at $2.7\,\mathrm{keV}$). The results are shown in Fig. 34. It can be seen that the peak position shifts towards larger values, in the case of enabled NL, due to the

recovering of charge information. For the photopeak, the relative shift is small, as the relative amount of recovered charge is small, while for the argon fluorescence peak the relative shift is larger. Furthermore, it can be seen that the width of the photopeak remains the same with or without NL, which is confirmed by the fit of the single Gaussian function (in both cases $\sigma \approx 140\,\mathrm{ADC\ Counts}$). This is expected because the relative fluctuations in the total charge and the amount of recovered charge due to the NL are small compared to the total charge collected. For the case of the argon fluorescence peak, this situation is different. Here, the relative fluctuations in the total charge and the loss of charge information due to the THL are larger for the case without NL, explaining that the $2.7\,\mathrm{keV}$ peak with NL enabled is narrower than the one without NL. Numerically, this means that the energy resolution R for the photopeak (FWHM) changes from $R_{\mathrm{wo}} = (24.0 \pm 0.3)\%$ (without NL) to $R_{\mathrm{nl}} = (22.8 \pm 0.3)\%$ (NL enabled). For the argon peak, the energy resolution changes significantly from $R_{\mathrm{wo}} = (53.4 \pm 0.7)\%$ to $R_{\mathrm{nl}} = (27.8 \pm 0.8)\%$. Although the experimental set-up was already adjusted to identify also events with low energy deposition, the difference in R for the $2.7\,\mathrm{keV}$ clusters may become smaller with a highly optimised experimental set-up. Nonetheless, these studies give a good indication of the advantages provided by the VMM3a's neighbouring-logic for the self-triggered readout of particle detectors in case of low energy deposition.

5. Conclusion

With the VMM3a's integration into RD51's Scalable Readout System (SRS), a powerful tool for the readout of MPGDs is provided. It combines, among other things, a self-triggered high-rate readout, an analogue part to access the energy deposited in a detector, a digital data output, as well as a so-called neighbouring-logic that allows to recover charge information at the tails of the clusters that are below the threshold level. In this article, we studied the capabilities of VMM3a/SRS by focusing on X-ray imaging, for which its features are of great interest. Particular attention was paid to the energy and position resolution and the advantages arising from the neighbouring-logic.

Due to the VMM3a's analogue part, the charge distribution of the clusters created by the incident radiation can be accessed, allowing a precise determination of the cluster position, e.g. with the Centre-Of-Gravity (COG) method is possible. The COG method may not be the ideal choice though for the position reconstruction in self-triggered readout systems, as charge information is lost due to the threshold level. This introduces a modulation of the discrete readout structure in the position reconstruction, of which we present an example in this article. We presented various methods to mitigate this modulation effect. The neighbouring-logic of the VMM3a was shown, where the goal is to reduce the modulation effect by better reconstructing the cluster's position as charge information can be recovered. We recalled
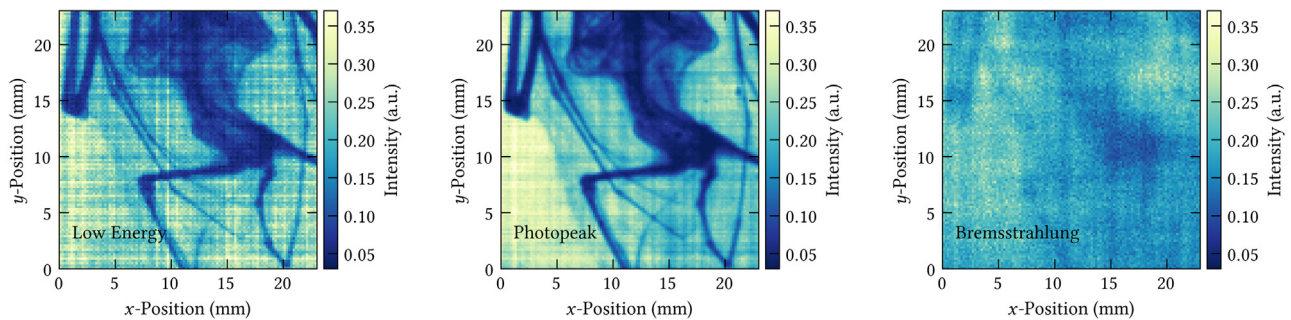
Fig. 33. Images of the bat for the different energy regimes. Here the Q^2 with NL was used for the position reconstruction.
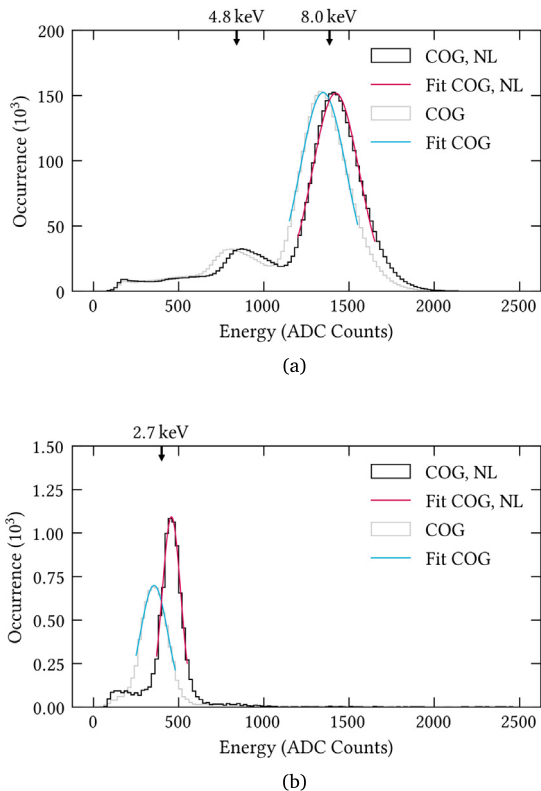

(a)

(b)

Fig. 34. In (a), the total energy spectrum of the copper X-rays is shown. In (b), the argon fluorescence peak with the Gaussian fit is shown. The annotated energy values are the expected ones and serve only for reference purposes.

the η-method, which is an iterative approach to reduce the modulation effect, based on the recorded events. We then discussed an empirical modification of the COG method, which is event-based and reduces the impact of the tails of the charge distribution by using the square of the charge as a weight when calculating the cluster positions.

With simple Monte Carlo methods and numerical calculations, as well as spatial resolution measurements using the modulation transfer function and the edge spread function, we investigated the impact of the neighbouring-logic on the position reconstruction. We confirmed that the charge is recovered by the neighbouring-logic, leading to an improvement in the position reconstruction. In addition, we explored the Q^2 weighting method. We derived that it can improve the position reconstruction in situations where COG is not ideal, but that its applicability depends on several parameters (threshold level, charge cloud width, readout structure). In case the width of the charge cloud in the detector is much smaller than the pitch of the readout strips, the Q^2 weighting methods 'over-corrects' and the position reconstruction gets worse.

Afterwards, we applied the findings to X-ray imaging studies, with a special focus on energy-resolved imaging and the advantages provided by the neighbouring-logic. We used the capabilities of VMM3a/SRS to resolve the interaction of low-energetic fluorescence photons in the detector volume. We showed that by enabling the NL, the measured energy resolution of $2.7\,\mathrm{keV}$ clusters gets significantly improved. The NL can be particularly useful for imaging with an energy-based event-selection requiring a large dynamic range (e.g. fluorescence imaging), but also for applications where the charge deposition in the detector is generally small and a large fraction of signal can be recovered from below the threshold level (e.g. cluster reconstruction of MIPs for the µTPC-method).

The measurements leading to these results have been performed with a COMPASS-like triple-GEM detector with strip readout. Nonetheless, it is possible to derive general remarks and conclusions for other detector and readout types. The neighbouring-logic enforces a specific detector mapping, where adjacent readout channels of the detector are connected to adjacent channels of the VMM3a. This works e.g. with strips or rectangular pads, where the charge along one dimension is completely integrated. For other geometries, e.g. square or hexagonal pads, the mapping between readout electrode and readout channel is limited and not applicable to all adjacent pads. For the position reconstruction it can be generally stated that, depending on the situation, neither COG nor Q^2 may be ideal. In fact, it should be evaluated for each specific situation, which is the best method to reconstruct the position.

We would like to recall, that all the measurements on the neighbouring-logic have been performed with X-rays. Future studies on its impact on the position resolution (also with the Q^2 weighting method and possibly complementarily with position correction methods like the η-method or the pad response function) will be performed with charged particles in a tracker, as it provides a reference position.

CRediT authorship contribution statement

L. Scharenberg: Conceptualization, Formal analysis, Investigation, Methodology, Writing - original draft. **J. Bortfeldt:** Formal analysis, Investigation, Validation, Writing - review & editing. **F. Brunbauer:** Resources, Writing - review & editing. **K. Desch:** Conceptualization, Supervision, Writing - review & editing. **F. Garcia:** Writing - review & editing. **M. Hracek:** Resources, Writing - review & editing. **D. Janssens:** Writing - review & editing. **M. Lisowska:** Writing - review & editing. **M. Lupberger:** Resources, Writing - review & editing. **H. Muller:** Resources, Writing - review & editing. **H. Natal da Luz:** Formal analysis, Resources, Writing - review & editing. **E. Oliveri:** Conceptualization, Formal analysis, Methodology, Supervision, Writing - review & editing. **D. Pfeiffer:** Formal analysis, Resources, Software, Writing - review & editing. **H. Pulkkinen:** Formal analysis, Methodology, Writing - review & editing. **L. Ropelewski:** Conceptualization, Project administration, Writing - review & editing. **J. Samarati:** Writing - review & editing. **M. van Stenis:** Resources, Writing - review & editing. **A. Utrobicic:** Writing - review & editing. **R. Veenhof:** Writing - review & editing.

Declaration of competing interest

Acknowledgments

References

[1] Special issue: Advances in detectors and applications for medicine, Nucl. Instrum. Methods Phys. Res. A 809 (2016) 1–176, http://dx.doi.org/10.1016/S0168-9002(15)01544-2.

[2] M. Titov, L. Ropelewski, Micro-pattern gaseous detector technologies and RD51 collaboration, Modern Phys. Lett. A 28 (2013) 1340022, http://dx.doi.org/10.1142/S0217732313400221.

[3] F.M. Brunbauer, MPGD applications outside high-energy physics, Presentation at the 6th International Conference on Micro Pattern Gaseous Detectors, La Rochelle, 2019, URL https://indico.cern.ch/event/757322/contributions/3325207/attachments/1840579/3018383/MPGDApplications_Brunbauer.pdf.

[4] S. Procz, et al., X-ray and gamma imaging with Medipix and Timepix detectors in medical research, Radiat. Meas. 127 (2019) 106104, http://dx.doi.org/10.1016/j.radmeas.2019.04.007.

[5] K. Akiba, et al., The Timepix Telescope for high performance particle tracking, Nucl. Instrum. Methods Phys. Res. A 723 (2013) 47–54, http://dx.doi.org/10.1016/j.nima.2013.04.060.

[6] R. Ballabriga, et al., An introduction to the Medipix family ASICs, Radiat. Meas. 136 (2020) 106271, http://dx.doi.org/10.1016/j.radmeas.2020.106271.

[7] M. Bianco, Micromegas detectors for the muon spectrometer upgrade of the ATLAS experiment, Nucl. Instrum. Methods Phys. Res. A 824 (2016) 496–500, http://dx.doi.org/10.1016/j.nima.2015.11.076, Frontier Detectors for Frontier Physics: Proceedings of the 13th Pisa Meeting on Advanced Detectors.

[8] C. Altunbas, et al., Construction, test and commissioning of the triple-gem tracking detector for compass, Nucl. Instrum. Methods Phys. Res. A 490 (2002) 177–203, http://dx.doi.org/10.1016/S0168-9002(02)00910-5.

[9] Y. Giomataris, et al., MICROMEGAS: a high-granularity position-sensitive gaseous detector for high particle-flux environments, Nucl. Instrum. Methods Phys. Res. A 376 (1996) 29–35, http://dx.doi.org/10.1016/0168-9002(96)00175-1.

[10] M. Alviggi, et al., Small-pads resistive micromegas, J. Instrum. (2017) C03077, http://dx.doi.org/10.1088/1748-0221/12/03/C03077.

[11] G. Iakovidis, VMM3a, an ASIC for tracking detectors, 2019, ATL-MUON-PROC-2019-009, URL http://cds.cern.ch/record/2693463.

[12] M. Lupberger, et al., Implementation of the VMM ASIC in the scalable readout system, Nucl. Instrum. Methods Phys. Res. A 903 (2018) 91–98, http://dx.doi.org/10.1016/j.nima.2018.06.046.

[13] S. Martoiu, et al., Development of the scalable readout system for micro-pattern gas detectors and other applications, J. Instrum. 8 (2013) C03015, http://dx.doi.org/10.1088/1748-0221/8/03/c03015.

[14] RD51 Collaboration, Development of micro-pattern gas detectors technologies, URL http://rd51-public.web.cern.ch/rd51-public/.

[15] S. Martoiu, et al., Front-end electronics for the scalable readout system of RD51, in: 2011 IEEE Nuclear Science Symposium Conference Record, 2011, pp. 2036–2038, http://dx.doi.org/10.1109/NSSMIC.2011.6154414.

[16] F. Sauli, GEM: A new concept for electron amplification in gas detectors, Nucl. Instrum. Methods Phys. Res. A 386 (1997) 531–534, http://dx.doi.org/10.1016/S0168-9002(96)01172-2.

[17] G.D. Geronimo, et al., VMM1 - An ASIC for micropattern detectors, in: 2012 IEEE Nuclear Science Symposium and Medical Imaging Conference Record, NSS/MIC, 2012, pp. 633–639, http://dx.doi.org/10.1109/NSSMIC.2012.6551184.

[18] A.C. Thompson, et al., X-Ray Data Booklet, Lawrence Berkeley National Laboratory, 2009.

[19] D. Pfeiffer, et al., vmm-sdat – VMM3a/SRS data analysis tool: Analysis software for VMM3a data, recorded with the SRS as PCAP or HDF5 files (GdGEM pipeline of the EFU), URL http://github.com/ess-dmsc/vmm-sdat.

[20] F. Piuz, R. Roosen, J. Timmermans, Evaluation of systematic errors in the avalanche localization along the wire with cathode strips read-out MWPC, Nucl. Instrum. Methods Phys. Res. 196 (1982) 451–462, http://dx.doi.org/10.1016/0029-554X(82)90113-6.

[21] G. Iakovidis, The Micromegas project for the ATLAS upgrade, J. Instrum. 8 (2013) C12007, http://dx.doi.org/10.1088/1748-0221/8/12/c12007.

[22] D. Pfeiffer, The µTPC method: improving the position resolution of neutron detectors based on MPGDs, J. Instrum. 10 (2015) P04004, http://dx.doi.org/10.1088/1748-0221/10/04/p04004.

[23] M. Villa, Developing and Evaluating New Micropattern Gas Detectors (Ph.D. thesis), University of Bonn, 2014, URL https://nbn-resolving.org/urn:nbn:de:hbz:5n-35522.

[24] J. Bortfeldt, The Floating Strip Micromegas Detector, Springer International Publishing, 2015.

[25] W. Blum, L. Rolandi, Particle Detection with Drift Chambers, Springer-Verlag Berlin Heidelberg, 1993.

[26] R. Diener, Study of Reconstruction Methods for a Time Projection Chamber with GEM Gas Amplification System (Ph.D. thesis), University of Hamburg, DESY-THESIS-2006-040, 2006, http://dx.doi.org/10.3204/DESY-THESIS-2006-040.

[27] G. Charpak, et al., Progress in high-accuracy proportional chambers, Nucl. Instrum. Methods 148 (1978) 471–482, http://dx.doi.org/10.1016/0029-554X(78)91028-5.

[28] G. Charpak, et al., High-accuracy localization of minimum ionizing particles using the cathode-induced charge centre-of-gravity read-out, Nucl. Instrum. Methods 167 (1979) 455–464, http://dx.doi.org/10.1016/0029-554X(79)90227-1.

[29] J. Bortfeldt, et al., PICOSEC: Charged particle timing at sub-25 picosecond precision with a Micromegas based detector, Nucl. Instrum. Methods Phys. Res. A 903 (2018) 317–325, http://dx.doi.org/10.1016/j.nima.2018.04.033.

[30] F. Sauli, Gaseous Radiation Detectors, Cambridge University Press, Cambridge, 2014.

[31] M.J. Berger, et al., XCOM: Photon Cross Sections Database, National Institute of Standards and Technology, Gaithersburg, 2010, http://dx.doi.org/10.18434/T48G6X.

[32] M. Tanabashi, et al., (Particle Data Group), Review of particle physics, Phys. Rev. D 98 (2018) 030001, http://dx.doi.org/10.1103/PhysRevD.98.030001.

[33] S. Biagi, Magboltz - transport of electrons in gas mixtures, URL http://magboltz.web.cern.ch/magboltz/.

[34] A. Maier, et al. (Eds.), Medical Imaging Systems, Springer International Publishing, 2018.

[35] S.N. Ahmed, Physics and Engineering of Radiation Detection, Elsevier, 2015.

[36] C. Azevedo, et al., Position resolution limits in pure noble gaseous detectors for X-ray energies from 1 to 60 keV, Phys. Lett. B 741 (2015) 272–275, http://dx.doi.org/10.1016/j.physletb.2014.12.054.

[37] S.W. Smith, Digital Signal Processing: A Practical Guide for Engineers and Scientists, Newnes, Boston, 2002.

[38] L. Scharenberg, et al., Resolving soft X-ray absorption in energy, space and time in gaseous detectors using the VMM3a ASIC and the SRS, Nucl. Instrum. Methods Phys. Res. A 977 (2020) 164310, http://dx.doi.org/10.1016/j.nima.2020.164310.